

Lone pair driven anisotropy in antimony chalcogenide semiconductors

Xinwei Wang,¹ Zhenzhu Li,^{1,2} Seán R. Kavanagh,^{1,3} Alex M. Ganose,¹ and Aron Walsh^{1,2, a)}

¹*Department of Materials, Imperial College London, Exhibition Road, London SW7 2AZ, UK*

²*Department of Materials Science and Engineering, Yonsei University, Seoul 03722, Korea*

³*Thomas Young Centre and Department of Chemistry, University College London, 20 Gordon Street, London WC1H 0AJ, UK*

(Dated: 27 October 2021)

Antimony sulfide (Sb_2S_3) and selenide (Sb_2Se_3) have emerged as promising earth-abundant alternatives among thin-film photovoltaic compounds. A distinguishing feature of these materials is their anisotropic crystal structures, which are composed of quasi-one-dimensional (1D) $[\text{Sb}_4\text{X}_6]_n$ ribbons. The interaction between ribbons has been reported to be van der Waals (vdW) in nature and Sb_2X_3 are thus commonly classified in the literature as 1D semiconductors. However, based on first-principles calculations, here we show that inter-ribbon interactions are present in Sb_2X_3 beyond the vdW regime. The origin of the anisotropic structures is related to the stereochemical activity of the Sb 5s lone pair according to electronic structure analysis. The impacts of structural anisotropy on the electronic, dielectric and optical properties relevant to solar cells are further examined, including the presence of higher dimensional Fermi surfaces for charge carrier transport. Our study provides guidelines for optimising the performance of Sb_2X_3 -based photovoltaics via device structuring based on the underlying crystal anisotropy.

I. INTRODUCTION

Solar photovoltaic (PV) technology which converts the solar energy into electricity provides a clean and sustainable solution to the energy crisis. Current commercial thin-film light absorber materials such as cadmium telluride (CdTe) and copper indium gallium selenide (CIGS) have achieved certified PV efficiencies of over 20% under laboratory conditions¹. However, CdTe suffers from the scarcity of Te elements and toxicity of Cd elements, while in CIGS the cost of In and Ga elements is too high, which limit their large-scale applications. As potential alternatives, antimony chalcogenides (Sb_2X_3 ; X=S, Se) have attracted growing attention. Sb_2X_3 have advantages of long-term stability, optimal bandgaps and high absorption coefficients ($>10^5 \text{ cm}^{-1}$) with abundant, non-toxic and low-cost constituents²⁻⁴. The PV conversion efficiencies of Sb_2X_3 devices have increased rapidly during the last decade. The current record efficiencies for pure Sb_2S_3 and Sb_2Se_3 have reached 7.5% and 9.2% respectively^{5,6}. However, these values are still far below the maximum theoretical efficiency of $\sim 30\%$ predicted by the Shockley–Queisser (SQ) model⁷ which is an idealised model only based on band gaps of solar absorbers.

Intensive efforts have been devoted to improve the efficiencies in Sb_2X_3 solar cells. One research direction is the orientation control of Sb_2X_3 films^{8,9}. Based on the understanding that Sb_2X_3 are composed of one-dimensional (1D) $[\text{Sb}_4\text{X}_6]_n$ ribbons which are held together by vdW forces¹⁰⁻¹⁴, it has been reported that higher PV efficiency could be achieved when the Sb_2X_3 films are oriented more perpendicular to the substrate due to more efficient

carrier transport along ribbons than between them¹⁵. Consequently, researchers have focused on tailoring the growth orientation of Sb_2X_3 films in order to achieve high efficiencies^{6,16-19}. However, the origin of anisotropic crystal structures and the connection to physical properties remains unclear. Building on recent work that has shown a tolerance to structural reconstructions²⁰, understanding how film orientations affect the conversion efficiency in Sb_2X_3 is crucial to designing high-performance devices.

In this study, we investigate the anisotropic structural, electronic and optical properties of Sb_2X_3 using first-principles calculations. The dimensionality of Sb_2X_3 is studied by consideration of the chemical binding energies, carrier effective masses, and Fermi surfaces. Electronic structure analysis further confirms that the anisotropic crystal structures of Sb_2X_3 result from the stereochemical activity of the Sb 5s lone pair. Moreover, anisotropic optical properties including dielectric constants and optical absorption spectra are reported.

II. METHODS

Analysis of the total energy and electronic structure was performed within the framework of Kohn-Sham density-functional theory (DFT)^{21,22}. Calculations were performed based on DFT as implemented in the Vienna Ab initio Simulation Package (VASP)²³. The projector augmented-wave (PAW) method²⁴ was employed with a plane-wave energy cutoff of 400 eV. All calculations were carried out using the Heyd-Scuseria-Ernzerhof hybrid functional (HSE06)^{25,26} except for the calculation of ionic contribution of dielectric constants, as a lower-level functional is sufficient for this high-cost calculation²⁷.

To account for the weak inter-ribbon interactions, the

^{a)}Electronic mail: a.walsh@imperial.ac.uk

optB86b-vdW functional²⁸ was used to calculate the ionic contribution to the static dielectric constant, and the D3 dispersion correction²⁹ was used for HSE06 calculations. The coefficients used for the zero-damping D3 correction are consistent with the previous research³⁰. In order to obtain well-converged structures, the atomic positions were optimised until the Hellman-Feynman forces on each atom were below $0.0005 \text{ eV } \text{\AA}^{-1}$, and the energy convergence criterion was set to 10^{-8} eV . According to convergence tests (shown in Table. S2), the total energies of Sb_2S_3 and Sb_2Se_3 converge to within 1 meV/atom at a k -point mesh of $7 \times 2 \times 2$. Therefore, Γ -centered k -point meshes were set to $7 \times 2 \times 2$ for geometry optimisation with primitive unit cells, and $14 \times 4 \times 4$ for projected density of states (PDOS) and crystal orbital Hamilton populations (COHP) calculations. For calculations of effective masses, dielectric constants and optical absorption coefficients which are more sensitive to k -point density, detailed settings and the proof of convergence are shown in the SI (Table S3-S6).

The crystal structures and partial charge densities were plotted using CrystalMaker^{®31}. The PDOS and optical absorption spectra were plotted using the sumo package³². COHP calculations were performed using the LOBSTER package³³. Fermi surfaces were plotted using the IFermi package³⁴. The conductivity effective mass tensors were calculated by the AMSET package³⁵. The conductivity effective mass (m^*) is obtained based on Boltzmann transport theory^{36,37} and is defined as³⁸:

$$\frac{1}{m^*} = \frac{\sigma}{ne^2\tau} \quad (1)$$

Where σ is the conductivity, n is the carrier concentration, e is the electron charge and τ is the carrier life time, in this work set to 10^{-14} s . The ionic contribution to the static dielectric constants was calculated by density functional perturbation theory (DFPT)³⁹, while the electronic part was calculated using the approach developed by Furthmüller et al.³⁹ The optical absorption coefficients (α) were calculated from the dielectric function by the sumo package³² using the equation:

$$\alpha(\omega) = \frac{4\pi}{\lambda} k(\omega) \quad (2)$$

Where ω and λ are the frequency and wavelength of the incident light, respectively. $k(\omega)$ is the extinction coefficient defined as

$$k(\omega) = \sqrt{\frac{\sqrt{\varepsilon_1^2 + \varepsilon_2^2} - \varepsilon_1}{2}} \quad (3)$$

Where ε_1 and ε_2 are the real and imaginary parts of the high-frequency dielectric constants, respectively. The figures of distance histograms, COHP, dielectric constants, optical absorption spectra and thickness-dependent maximum efficiencies were plotted using matplotlib⁴⁰.

III. RESULTS AND DISCUSSIONS

A. Structural properties

The ground-state crystal structures of Sb_2S_3 and Sb_2Se_3 ($Pnma$ space group) are shown in Fig. 1a. They are composed of strongly bonded quasi-1D $[\text{Sb}_4\text{X}_6]_n$ ribbons units stacked together by weak interactions. In order to better reproduce the crystal structures, different vdW dispersion correction methods were applied in the geometry optimisation process. Lattice parameters calculated by different functionals and different vdW correction methods and obtained by experiments^{41–46} are shown in Table I. The c parameter (the direction between ribbons) is significantly overestimated ($> 7.0\%$) with no dispersion correction included for both PBE and HSE06 functionals. Including dispersion corrections, the accuracy of lattice parameter in the c direction is greatly improved regardless of the correction methods. This demonstrates the presence of significant vdW interactions between ribbons, which are much weaker than the bonding within ribbons, and thus the necessity of dispersion corrections when modelling Sb_2X_3 . For both systems, HSE06+D3 gives the best agreement with experimental measurements (an average difference of 0.7% and 0.9% for Sb_2S_3 and Sb_2Se_3 from the experimental lattice constants, respectively), which is in agreement with previous studies^{30,47}, followed by optB86b performing the next best (1.0% and 1.4% difference for Sb_2S_3 and Sb_2Se_3 , respectively). Thus, the HSE06 functional with the D3 Grimme dispersion correction was used for most of the following calculations and the optB86b functional was used for most convergence tests.

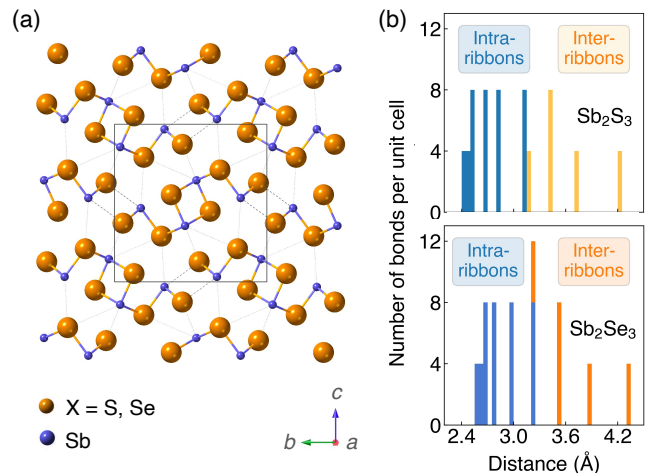


FIG. 1: (a) Crystal structures ($Pnma$ space group) and (b) histogram of Sb-X distances of Sb_2S_3 and Sb_2Se_3 . The unit cells are represented by rectangles.

Histograms of distances between Sb and X ions are shown in Fig. 1b. The widely distributed bond lengths

TABLE I: Lattice parameters (\AA) of Sb_2S_3 and Sb_2Se_3 as calculated by different functionals and different vdW dispersion correction methods. The percentage error (%) relative to the experimental average is given in parentheses

| System | PBE | PBE+D3 | PBE+TS | optB86b | HSE06 | HSE06+D3 | HSE06+TS | Experimental data | | | | |
|--------------------------|-----|-----------------|-----------------|-----------------|-----------------|----------------|-----------------|-------------------|---------------|---------------|---------|-------|
| | | | | | | | | Ref. [41, 42] | Ref. [43, 44] | Ref. [45, 46] | Average | |
| Sb_2S_3 | a | 3.87 (1.0) | 3.84 (0.3) | 3.88 (1.3) | 3.86 (0.8) | 3.80 (-0.8) | 3.80 (-0.8) | 3.81 (-0.5) | 3.84 | 3.82 | 3.84 | 3.83 |
| | b | 11.22 (-0.4) | 10.92 (-3.1) | 11.09 (-1.5) | 11.04 (-2.0) | 11.39 (1.1) | 11.20 (-0.5) | 11.22 (-0.4) | 11.22 | 11.27 | 11.29 | 11.26 |
| | c | 12.14 (7.0) | 11.15 (-1.3) | 11.54 (2.2) | 11.32 (0.3) | 12.09 (6.6) | 11.39 (0.9) | 11.54 (2.2) | 11.31 | 11.30 | 11.27 | 11.29 |
| Sb_2Se_3 | a | 4.03 (1.2) | 3.99 (0.3) | 4.04 (1.5) | 4.02 (1.0) | 3.96 (-0.5) | 3.95 (-0.8) | 3.97 (-0.3) | 3.98 | 3.99 | 3.96 | 3.98 |
| | b | 11.53 (-1.0) | 11.33 (-2.7) | 11.41 (-2.0) | 11.46 (-1.6) | 11.73 (0.8) | 11.55 (-0.8) | 11.54 (-0.9) | 11.65 | 11.65 | 11.62 | 11.64 |
| | c | 12.84 (8.2) | 11.68 (-0.9) | 12.31 (4.2) | 11.90 (0.9) | 12.65 (6.8) | 11.93 (1.2) | 12.18 (3.2) | 11.80 | 11.79 | 11.77 | 11.79 |

indicate the anisotropic connectivity of Sb_2X_3 . The bond lengths of Sb_2Se_3 are slightly larger than those of Sb_2S_3 due to the increased anion radius. In the study of Deringer et al⁴⁸, analysis of the integrated COHP and the harmonic force constants showed a clear separation between strong intra-ribbon and weaker inter-ribbon interactions in Sb_2Se_3 . In order to quantify the interaction between ribbons, inter-ribbon binding energies (E_b) (per unit cell) along the b and c directions are calculated by

$$E_{b(b)} = (E_{1D} - E_{2D})/2 \quad (4)$$

$$E_{b(c)} = (2E_{2D} - E_t)/N \quad (5)$$

where E_{1D} and E_{2D} are total energies of one 1D $[\text{Sb}_4\text{X}_6]_n$ ribbon in isolation and one 2D $[\text{Sb}_4\text{X}_6]_n$ ribbon periodically repeated along a and b directions, respectively (the 1D and 2D substructures are given in Fig. S1). E_t is the total energy of the unit cell. The parameter 2 in Eq. 5 is due to the fact that one unit cell of Sb_2X_3 contains two $[\text{Sb}_4\text{X}_6]_n$ ribbons. Note that the substructures were directly taken from the optimised structures and kept unrelaxed in order to avoid structural distortion effects, as is typical for binding energy calculations^{49,50}. The effect of optimisation was also tested and the E_b was ~ 0.1 eV lower after the relaxation of substructures, which does not qualitatively influence the results. The choice of N depends on whether $E_{b(c)}$ is defined as per atom or per bond. Table II shows the calculated E_b using the HSE06 functional and D3 dispersion correction. It can be seen that E_b of Sb_2S_3 and Sb_2Se_3 are both over $10 \text{ kJ}\cdot\text{mol}^{-1}$, which are both beyond the typical vdW regime ($0.4 \sim 4 \text{ kJ}\cdot\text{mol}^{-1}$)⁵¹. This is consistent with previous research that the distance of Sb-S between ribbons in Sb_2S_3 is shorter than the sum of Sb and S vdW radii at 293 K⁴¹. Moreover, $E_{b(b)}$ is larger than $E_{b(c)}$ due to the elongation of ribbons along b , and the E_b of Sb_2Se_3 is slightly larger than that of Sb_2S_3 . The calculated values agree well with previous calculations⁵² and indicate that the inter-ribbon interactions of Sb_2S_3 and Sb_2Se_3 are both

between the vdW and covalent regime. The results of E_b without vdW corrections are given in Table S1.

TABLE II: Inter-ribbon binding energies ($\text{kJ}\cdot\text{mol}^{-1}$) of Sb_2S_3 and Sb_2Se_3

| System | $E_{b(b)}$ | | $E_{b(c)}$ | |
|--------------------------|------------|-----------------|-----------------|--|
| | per bond | per bond (N=16) | per atom (N=20) | |
| Sb_2S_3 | 27.44 | 15.96 | 12.77 | |
| Sb_2Se_3 | 31.13 | 17.95 | 14.36 | |

B. Electronic properties

The strength of the interaction between ribbons is closely related to the distortion of Sb which originates from the stereochemically active Sb $5s$ lone pairs. Before going further into the lone pair analysis, the density of states and orbital overlaps are first investigated.

The PDOS are shown in Fig. 2a and 2b. The valence band (VB) can be divided into two main parts. The highest occupied VB between -1 and 0 eV consists of S $3p$ /Se $4p$, Sb $5s$ and Sb $5p$ states. While the states between -10 and -7 eV mainly consists of Sb $5s$ orbitals, alongside some small contributions from S $3s$ /Se $4s$ and S $3p$ /Se $4p$ states. A valley at about 2 eV below the valence band maximum (VBM) is demonstrated to be one of the major characteristics of energy distribution curves for Sb_2Se_3 according to the photoemission measurements⁴⁶. Our calculated PDOS of Sb_2Se_3 also shows a valley at ~ -2 eV which is in good agreement with the experimental results. The conduction band (CB) are dominated by Sb $5p$ and S $3p$ /Se $4p$ states. These results agree well with earlier studies of PDOS on Sb_2X_3 ^{48,53-55}.

The bonding and antibonding interactions are further studied by COHP³³ (shown in Fig. 2c and 2d). Two separate cases are plotted since Sb has two distinct chemical environment. The interaction is weaker in Sb(1)-X(1) than Sb(2)-X(2) which agrees with the longer bond

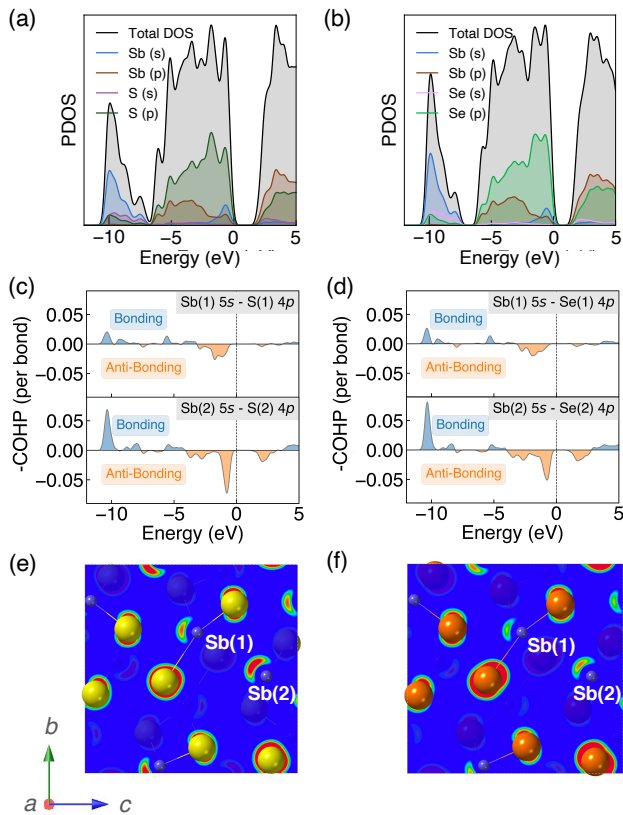


FIG. 2: (a)-(b) Projected density of states (PDOS), (c)-(d) crystal orbital Hamilton populations (COHP) and (e)-(f) partial charge densities of antimony chalcogenides. The range of isosurface value for partial charge densities is set to $0.05 \sim 0.10 e/\text{\AA}^3$ for both Sb_2S_3 and Sb_2Se_3 . The valence band maximum (VBM) is set to 0.

lengths of $\text{Sb}(1)\text{-X}(1)$. Combined with the results of PDOS, the energy range from -10 to -7 eV corresponds to a bonding interaction between $\text{Sb } 5s$ and $\text{S } 3p/\text{Se } 4p$ states, whereas the region at the top of the VB corresponds to an antibonding state, which is similar to other quasi-1D systems with stereochemically active lone pairs⁵⁶. The photoemission measurements for Sb_2Se_3 ⁴⁶ show that the lower part of VB below ~ -6 eV is contributed by bonding states which agrees well with our results. Moreover, the interaction is stronger in Sb_2S_3 than Sb_2Se_3 which will be discussed in detail later.

The different inter-ribbon interactions in Sb_2S_3 and Sb_2Se_3 result from the $\text{Sb } 5s$ lone pair formation. In the revised lone pair model⁵⁷, the interaction between the antibonding states of cation s - anion p and cation p states results in the formation of stereochemically active lone pairs. Smaller energy difference between cation s and anion p states will facilitate stronger interaction and thus stronger lone pair formation. In our systems, for the $\text{Sb}(\text{III})$ oxidation state found in Sb_2X_3 , the formal electronic configuration of Sb is $5s^25p^0$. Based on the

discussions above, the $\text{Sb } 5s$ states interact with the $\text{S } 3p/\text{Se } 4p$ states in the VB forming filled bonding and anti-bonding states. The additional interaction of the nominally empty $\text{Sb } 5p$ orbitals stabilises the system by lowering the total energy, which is similar to other lone pair systems⁵⁷⁻⁶⁰. The resulting stereochemically active lone pair results in an asymmetric electronic density at the top of VB which can be visualised by the contour plot of partial charge density. Partial charge densities for the states between -1 and 0 eV (with respect to the VBM) are shown in Fig. 2e and 2f. They are obtained by cutting the (100) plane through Sb atoms. The lone pair is stronger in Sb_2S_3 compared with Sb_2Se_3 due to the smaller energy separation and increased overlap of $\text{Sb } 5s$ and $\text{S } 3p$.

To connect the electronic structure to transport properties, effective masses of electrons and holes were calculated (shown in Table III). According to the electronic band structures of Sb_2S_3 and Sb_2Se_3 (shown in Fig. S2), the band dispersions around the extrema are relatively flat which are far from parabolic, and several extrema in different parts of the Brillouin Zone which are close in energy could be involved in contributing to conductivity. Therefore, effective masses in Sb_2X_3 are quite sensitive to calculation parameters (particularly the k -point density), and effective masses larger than 2 are rounded to the nearest whole numbers in Table III and S3. The harmonic mean is used to average the values for a polycrystalline sample with random orientations, and the anisotropy ratio (a_r) is defined as the ratio of maximum to minimum effective mass. The average effective masses of holes are larger than those of electrons for both Sb_2S_3 and Sb_2Se_3 , indicating that Sb_2S_3 and Sb_2Se_3 may be better n-type semiconductors. Nevertheless, the electron effective masses show a stronger anisotropy. a_r is larger in Sb_2Se_3 than Sb_2S_3 for both electron and hole effective masses, suggesting Sb_2Se_3 has stronger anisotropy which agrees with the weaker lone pair in Sb_2Se_3 . The electron and hole effective masses are the largest along [001] for both Sb_2S_3 and Sb_2Se_3 , indicating the conductivity between ribbons will be lower than along the other two directions. In general the values follow the trend $x < y < z$, with the exception of the hole effective mass for Sb_2Se_3 , which is discussed later. Moreover, the 2D nature of transport (with small effective masses in two directions and large effective mass in the other direction) is similar to other so-called “quasi-1D” systems such as BiSI and BiSeI ⁶¹. Our calculated effective masses deviate largely from other studies on Sb_2X_3 ^{62,63}. One possible reason of the discrepancy could be the use of simple parabolic fitting or the consideration of solely the Γ point in other computational investigations. The choice of functionals could be another important factor, as demonstrated by Whalley et al.⁶⁴ It has been demonstrated that semi-local functionals would not only underestimate the bandgap, but also would influence the shape of band structures, resulting in overestimated nonparabolicity.

To further illustrate the dimensionality of the elec-

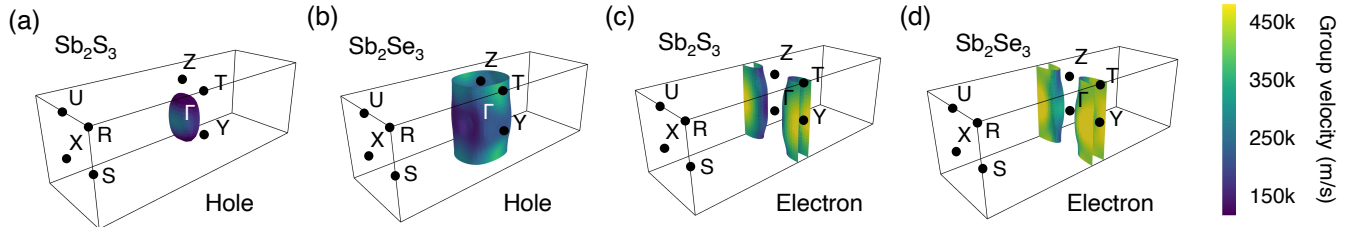


FIG. 3: Fermi surfaces of Sb_2S_3 and Sb_2Se_3 . (a) and (c) are hole Fermi surfaces (0.1 eV below the valence band maximum (VBM)), while (b) and (d) are electron Fermi surfaces (0.1 eV above the conduction band minimum (CBM)). The different colors represent the magnitude of group velocity (m/s)

TABLE III: Effective masses of Sb_2S_3 and Sb_2Se_3 . The harmonic mean is represented by \bar{m}^* . The anisotropy ratio (a_r) is defined as the ratio of maximum to minimum effective mass.

| System | | x | y | z | \bar{m}^* | a_r |
|--------------------------|-------------|------|------|------|-------------|-------|
| Sb_2S_3 | m_e^*/m_0 | 0.16 | 0.92 | 5 | 0.40 | 31.25 |
| | m_h^*/m_0 | 0.47 | 0.65 | 0.97 | 0.64 | 2.06 |
| Sb_2Se_3 | m_e^*/m_0 | 0.14 | 0.81 | 7 | 0.35 | 50.00 |
| | m_h^*/m_0 | 0.85 | 0.55 | 3 | 0.90 | 5.45 |

tronic structure, Fermi surfaces were plotted at 0.1 eV below (above) the VBM (CBM) using the IFermi package³⁴ (shown in Fig. 3). 0.1 eV is an arbitrary value intended to indicate the shape of the Fermi surface close to the band edge. Due to the tails of the Fermi-Dirac distribution, this energy range will be occupied at room temperature and the Fermi surface is therefore reflective of the states that govern transport properties. The Fermi surfaces of 0.08 and 0.12 eV below (above) the valence band maximum (conduction band maximum) were also shown in Fig. S3 and S4 which qualitatively show the same behaviour. An ellipsoidal Fermi surface is found for holes in Sb_2S_3 (Fig. 3a), indicating dispersion in three dimensions⁶⁵. The shape of elliptical cylinders found for electrons in Sb_2S_3 (Fig. 3c) can be classified as quasi-2D with small dispersion in the [001] direction⁶⁵. These agree well with observation that the hole effective mass of Sb_2S_3 is much smaller than the electron effective mass in the [001] direction. In contrast, the hole and electron Fermi surfaces of Sb_2Se_3 are both quasi-2D (shown in Fig. 3b and 3d). It can be seen that the electron Fermi surfaces of Sb_2S_3 and Sb_2Se_3 have similar topology, which indicates similar transport behaviour, whereas their hole Fermi surfaces have a significant difference in terms of the dimensionality. Indeed, for Sb_2S_3 the three components of the effective mass are all below one, while for Sb_2Se_3 the z component is greater than 3. We link this behaviour to the stronger lone pair distortion of Sb_2S_3 and the resulting shorter inter-ribbon Sb-S bonds along the [001] direction.

C. Optical properties

The dielectric constants are important descriptors for the optical properties of crystals. The static dielectric constant (ϵ_0) is defined as the sum of the ionic and high-frequency response to an external electric field. The complex dielectric function $\epsilon(\omega)$ is given by:

$$\epsilon(\omega) = \epsilon_1(\omega) + i\epsilon_2(\omega) \quad (6)$$

Where ϵ_1 and ϵ_2 are the real part and imaginary part of the frequency-dependent dielectric function, respectively. For orthorhombic structures, the dielectric tensor has three distinct non-zero components. As shown in Table IV, the dielectric constants of Sb_2X_3 are anisotropic and relatively large, which is common in lone-pair containing crystals^{56,60}. Large dielectric constants indicate the potential for strong screening to charged defects and low recombination losses^{66,67}. It can be seen that the dielectric constants are larger in the x and y directions than the z direction, indicating the screening is stronger in the ab plane. Moreover, the dielectric screening in Sb_2X_3 is shown to be dominated by the lattice polarization as the ionic contribution is much larger than the electronic contribution. The large ionic dielectric constants can be attributed to large Born effective charges in Sb_2X_3 ^{68,69}. The anisotropy ratio (a_r) (defined as the ratio of maximum to minimum dielectric constant) is larger in Sb_2Se_3 than Sb_2S_3 for both static and high-frequency dielectric constants, indicating Sb_2Se_3 has stronger anisotropy which is consistent with previous discussions.

The real and imaginary parts of the high-frequency (ϵ_∞) dielectric functions are plotted in Fig. 4. Combined with the results of PDOS, the peaks in the imaginary parts of dielectric functions mainly correspond to the optical transition from the S 3p/Se 4p states in the valence band to the Sb 5p states in the conduction band. Our calculated dielectric constants are in excellent agreement with ellipsometry measurements on polycrystalline thin films ($\epsilon_{\infty,x}$, $\epsilon_{\infty,y}$ and $\epsilon_{\infty,z}$ of 12.5, 10.8 and 7.0 for Sb_2S_3 ⁷⁰, respectively, and an averaged ϵ_∞ of 14.3 for Sb_2Se_3 ²). Furthermore, our results are inline with previous theoretical studies^{54,71-74}.

The calculated optical absorption spectra, and upper

TABLE IV: Calculated static (ϵ_0) and high-frequency (ϵ_∞) dielectric constants of Sb_2S_3 and Sb_2Se_3 . The anisotropy ratio (a_r) is defined as the ratio of maximum to minimum dielectric constant.

| System | ϵ_0 | | | | ϵ_∞ | | | |
|--------------------------|--------------|--------|-------|-------|-------------------|-------|-------|-------|
| | x | y | z | a_r | x | y | z | a_r |
| Sb_2S_3 | 98.94 | 94.21 | 13.14 | 7.53 | 11.55 | 10.97 | 8.25 | 1.40 |
| Sb_2Se_3 | 85.64 | 128.18 | 15.00 | 8.54 | 15.11 | 14.92 | 10.53 | 1.43 |

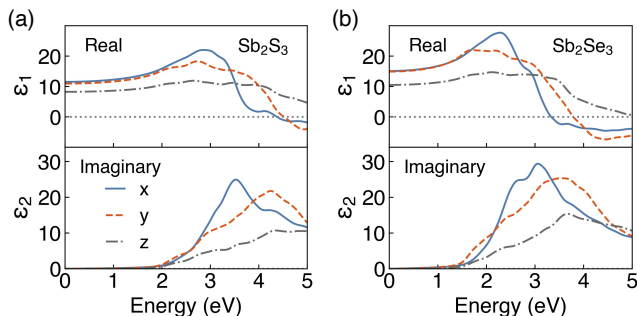


FIG. 4: Calculated high-frequency dielectric functions of (a) Sb_2S_3 and (b) Sb_2Se_3 .

limit to photovoltaic efficiency, for Sb_2S_3 and Sb_2Se_3 are shown in Fig. 5. As can be seen in Fig. 5a, both Sb_2S_3 and Sb_2Se_3 possess high optical absorption coefficients above the band edge (in the range of 10^5 cm^{-1}) which could more effectively absorb photons and generate electron-hole pairs. This agrees well with experimental UV-vis measurements on Sb_2X_3 , which observed large absorption coefficients of $\sim 10^5 \text{ cm}^{-1}$ in the visible region^{4,66,75,76}. Possible reasons for such high optical absorption coefficients in these indirect gap semiconductors could be attributed to their unique electronic band structures (shown in Fig. S2). On the one hand, the difference between indirect and direct gaps of Sb_2X_3 is small (0.16 eV for Sb_2S_3 and 0.06 eV for Sb_2Se_3) which make them still suitable for strong absorption near the band edges⁷⁷. On the other hand, the relatively flat dispersions near the band extrema will lead to high DOS near the VBM and CBM and thus strong absorption⁷⁸. Moreover, there is slight difference in absorption coefficients along different directions. The thickness-dependent radiative efficiencies (Fig. 5b) further show the same trend regardless of different orientations, which results from the relatively large absorption coefficients and the same value of the optical band gap along different directions. The radiative efficiencies are larger in Sb_2Se_3 than Sb_2S_3 since the band gap of Sb_2Se_3 is closer to the optimal band gap predicted by the SQ model. For both Sb_2S_3 and Sb_2Se_3 , the radiative efficiencies approach the SQ limit at a thickness of 2 μm . The results above indicate that absorption is not a limiting factor in the conversion efficiencies along different directions in Sb_2S_3 and Sb_2Se_3 . Other effects such as defects and interfaces should be further considered in

order to improve the efficiency in Sb_2X_3 .

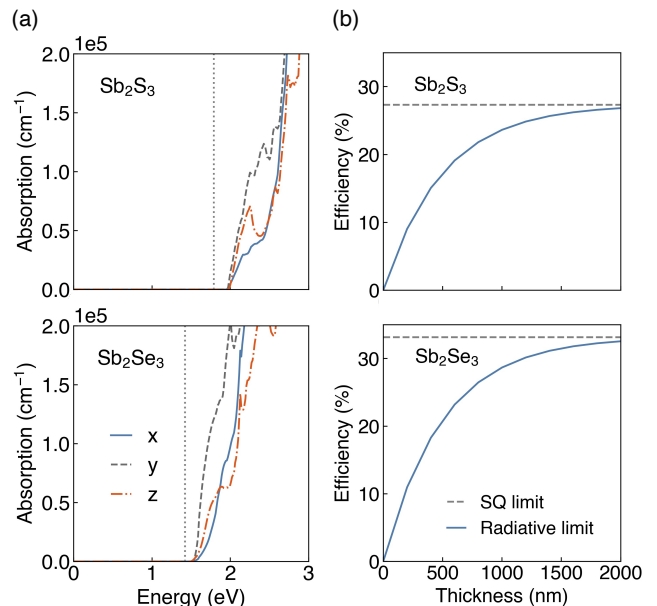


FIG. 5: (a) Calculated optical absorption spectra of Sb_2S_3 and Sb_2Se_3 . The fundamental band gaps are shown in grey dotted lines. (b) Thickness-dependent maximum efficiencies based on the radiative limit of Sb_2S_3 and Sb_2Se_3 .

IV. CONCLUSIONS

The standard description of Sb_2X_3 in the literature refers to them as 1D semiconductors, where electrons and holes can readily diffuse *along*, but not *between*, ribbons in the crystal. This has led to a focus on thin-film synthesis to achieve optimal [100] orientations. Our first-principles investigation has shown that the chemical binding energies between ribbons ($>10 \text{ kJ}\cdot\text{mol}^{-1}$) falls between the vdW and ionic/covalent regime. Analysis of the carrier effective masses does reveal a strong anisotropy, but the behaviour is not 1D, with stronger dispersion found in [010] compared to [001]. The Fermi surfaces for electrons and holes illustrate this complexity with a combination of 3D (holes in Sb_2S_3) and quasi-2D transport. The anisotropy carries through to the dielectric response of the crystals with much stronger screening in the ab plane compared to along the c axis. However, the resulting optical absorption profiles are less sensitive and yield the same radiative limit for photovoltaic applications. The origin of these anisotropic effects is linked to lone pair formation associated with the filled Sb $5s$ orbitals which distorts the Sb coordination environment.

ACKNOWLEDGEMENTS

We are grateful to the UK Materials and Molecular Modelling Hub for computational resources, which is partially funded by EPSRC (EP/P020194/1 and EP/T022213/1). Xinwei Wang acknowledges Imperial College London for the funding of a President's PhD Scholarship. Seán R. Kavanagh acknowledges the EPSRC Centre for Doctoral Training in the Advanced Characterisation of Materials (CDT-ACM)(EP/S023259/1) for funding a PhD studentship. Alex M. Ganose was supported by EPSRC Fellowship EP/T033231/1. Xinwei Wang thanks Chengcheng Xiao and Sunghyun Kim for advice on the computational analysis.

DATA AVAILABILITY

The data that support the findings of this study are available in an online repository at <https://doi.org/10.5281/zenodo.XXX>.

REFERENCES

- ¹M. A. Green, E. D. Dunlop, J. Hohl-Ebinger, M. Yoshita, N. Kopidakis and A. W. Ho-Baillie, *Progress in Photovoltaics: Research and Applications*, 2020, **28**, 3–15.
- ²C. Chen, W. Li, Y. Zhou, C. Chen, M. Luo, X. Liu, K. Zeng, B. Yang, C. Zhang, J. Han *et al.*, *Appl. Phys. Lett.*, 2015, **107**, 043905.
- ³C. Ghosh and B. Varma, *Thin solid films*, 1979, **60**, 61–65.
- ⁴Y. Zhou, M. Leng, Z. Xia, J. Zhong, H. Song, X. Liu, B. Yang, J. Zhang, J. Chen, K. Zhou *et al.*, *Adv. Energy Mater.*, 2014, **4**, 1301846.
- ⁵Y. C. Choi, D. U. Lee, J. H. Noh, E. K. Kim and S. I. Seok, *Adv. Funct. Mater.*, 2014, **24**, 3587–3592.
- ⁶Z. Li, X. Liang, G. Li, H. Liu, H. Zhang, J. Guo, J. Chen, K. Shen, X. San, W. Yu *et al.*, *Nat. Commun.*, 2019, **10**, 1–9.
- ⁷W. Shockley and H. J. Queisser, *J. Appl. Phys.*, 1961, **32**, 510–519.
- ⁸J. Kim, S. Ji, Y. Jang, G. Jeong, J. Choi, D. Kim, S.-W. Nam and B. Shin, *Sol. RRL*, 2021, **5**, 2100327.
- ⁹T. D. Hobson, L. J. Phillips, O. S. Hutter, H. Shiel, J. E. Swallow, C. N. Savory, P. K. Nayak, S. Mariotti, B. Das, L. Bowen *et al.*, *Chem. Mater.*, 2020, **32**, 2621–2630.
- ¹⁰F. Caruso, M. R. Filip and F. Giustino, *Phys. Rev. B*, 2015, **92**, 125134.
- ¹¹H. Song, T. Li, J. Zhang, Y. Zhou, J. Luo, C. Chen, B. Yang, C. Ge, Y. Wu and J. Tang, *Adv. Mater.*, 2017, **29**, 1700441.
- ¹²L. Guo, B. Zhang, Y. Qin, D. Li, L. Li, X. Qian and F. Yan, *Sol. RRL*, 2018, **2**, 1800128.
- ¹³W. Yang, J. Ahn, Y. Oh, J. Tan, H. Lee, J. Park, H.-C. Kwon, J. Kim, W. Jo, J. Kim *et al.*, *Adv. Energy Mater.*, 2018, **8**, 1702888.
- ¹⁴R. Gusmão, Z. Sofer, J. Luxa and M. Pumera, *ACS Sustain. Chem. Eng.*, 2019, **7**, 15790–15798.
- ¹⁵Y. Zhou, L. Wang, S. Chen, S. Qin, X. Liu, J. Chen, D.-J. Xue, M. Luo, Y. Cao, Y. Cheng *et al.*, *Nat. Photonics*, 2015, **9**, 409–415.
- ¹⁶S. Yuan, H. Deng, D. Dong, X. Yang, K. Qiao, C. Hu, H. Song, H. Song, Z. He and J. Tang, *Sol. Energy Mater. Sol. Cells*, 2016, **157**, 887–893.
- ¹⁷L. Wang, D.-B. Li, K. Li, C. Chen, H.-X. Deng, L. Gao, Y. Zhao, F. Jiang, L. Li, F. Huang *et al.*, *Nat. Energy*, 2017, **2**, 1–9.
- ¹⁸R. Kondrotas, J. Zhang, C. Wang and J. Tang, *Sol. Energy Mater. Sol. Cells*, 2019, **199**, 16–23.
- ¹⁹Y. Zeng, K. Sun, J. Huang, M. P. Nielsen, F. Ji, C. Sha, S. Yuan, X. Zhang, C. Yan, X. Liu *et al.*, *ACS Appl. Mater. Interfaces*, 2020, **12**, 22825–22834.
- ²⁰K. P. McKenna, *Adv. Electron. Mater.*, 2021, **7**, 2000908.
- ²¹W. Kohn and L. J. Sham, *Phys. Rev.*, 1965, **140**, A1133.
- ²²R. M. Dreizler and E. K. Gross, *Density Functional Theory*, Springer, 1990, pp. 245–271.
- ²³G. Kresse and J. Furthmüller, *Phys. Rev. B*, 1996, **54**, 11169.
- ²⁴G. Kresse and D. Joubert, *Phys. Rev. B*, 1999, **59**, 1758.
- ²⁵J. Heyd, G. E. Scuseria and M. Ernzerhof, *J. Chem. Phys.*, 2003, **118**, 8207–8215.
- ²⁶A. V. Krukau, O. A. Vydrov, A. F. Izmaylov and G. E. Scuseria, *J. Chem. Phys.*, 2006, **125**, 224106.
- ²⁷S. R. Kavanagh, A. Walsh and D. O. Scanlon, *ACS Energy Lett.*, 2021, **6**, 1392–1398.
- ²⁸J. Klimeš, D. R. Bowler and A. Michaelides, *Phys. Rev. B*, 2011, **83**, 195131.
- ²⁹S. Grimme, *J. Comput. Chem.*, 2004, **25**, 1463–1473.
- ³⁰C. N. Savory and D. O. Scanlon, *J. Mater. Chem. A*, 2019, **7**, 10739–10744.
- ³¹*CrystalMaker, CrystalMaker Software Ltd, Oxford, England, (www.crystallmaker.com)*.
- ³²A. M. Ganose, A. J. Jackson and D. O. Scanlon, *J. Open Source Softw.*, 2018, **3**, 717.
- ³³R. Dronskowski and P. E. Blöchl, *J. Phys. Chem.*, 1993, **97**, 8617–8624.
- ³⁴A. M. Ganose, A. Searle, A. Jain and S. M. Griffin, *J. Open Source Softw.*, 2021, **6**, 3089.
- ³⁵A. M. Ganose, J. Park, A. Faghaninia, R. Woods-Robinson, K. A. Persson and A. Jain, *Nat. Commun.*, 2021, **12**, 1–9.
- ³⁶N. W. Ashcroft, N. D. Mermin *et al.*, *Solid State Physics*, 1976.
- ³⁷G. K. Madsen and D. J. Singh, *Comput. Phys. Commun.*, 2006, **175**, 67–71.
- ³⁸Z. M. Gibbs, F. Ricci, G. Li, H. Zhu, K. Persson, G. Ceder, G. Hautier, A. Jain and G. J. Snyder, *NPJ Comput. Mater.*, 2017, **3**, 1–7.
- ³⁹M. Gajdoš, K. Hummer, G. Kresse, J. Furthmüller and F. Bechstedt, *Phys. Rev. B*, 2006, **73**, 045112.
- ⁴⁰J. D. Hunter, *Comput. Sci. Eng.*, 2007, **9**, 90–95.
- ⁴¹A. Kyoono, M. Kimata, M. Matsuhisa, Y. Miyashita and K. Okamoto, *Phys. Chem. Miner.*, 2002, **29**, 254–260.
- ⁴²O. Savadogo and K. Mandal, *Sol. Energy Mater. Sol. Cells*, 1992, **26**, 117–136.
- ⁴³A. Salem and M. S. Selim, *J. Phys. D*, 2001, **34**, 12.
- ⁴⁴I. Efthimiopoulos, J. Zhang, M. Kucway, C. Park, R. C. Ewing and Y. Wang, *Sci. Rep.*, 2013, **3**, 1–8.
- ⁴⁵G. Voutsas, A. Papazoglou, P. Rentzeperis and D. Siapakas, *Z. Kristallogr. Cryst. Mater.*, 1985, **171**, 261–268.
- ⁴⁶Z. Hurych, D. Davis, D. Buczek, C. Wood, G. Lapeyre and A. Baer, *Phys. Rev. B*, 1974, **9**, 4392.
- ⁴⁷A. Stolaroff, A. Lecomte, O. Rubel, S. Jobic, X. Zhang, C. Latouche and X. Rocquefelte, *ACS Appl. Energy Mater.*, 2020, **3**, 2496–2509.
- ⁴⁸V. L. Deringer, R. P. Stoffel, M. Wuttig and R. Dronskowski, *Chem. Sci.*, 2015, **6**, 5255–5262.
- ⁴⁹N. Mounet, M. Gibertini, P. Schwaller, D. Campi, A. Merky, A. Marrazzo, T. Sohier, I. E. Castelli, A. Cepellotti, G. Pizzi *et al.*, *Nat. Nanotechnol.*, 2018, **13**, 246–252.
- ⁵⁰T. Björkman, A. Gulans, A. V. Krasheninnikov and R. M. Nieminen, *Phys. Rev. Lett.*, 2012, **108**, 235502.
- ⁵¹R. H. Garrett and C. M. Grisham, *Biochemistry*, 1999.
- ⁵²M. R. Filip, C. E. Patrick and F. Giustino, *Phys. Rev. B*, 2013, **87**, 205125.
- ⁵³R. Caracas and X. Gonze, *Phys. Chem. Miner.*, 2005, **32**, 295–300.

- ⁵⁴H. Koç, A. M. Mamedov, E. Deligoz and H. Ozisik, *Solid State Sci.*, 2012, **14**, 1211–1220.
- ⁵⁵A. Radzwan, R. Ahmed, A. Shaari, A. Lawal and Y. X. Ng, *Malays. J. Fundam. Appl. Sci.*, 2017, **13**, 285–289.
- ⁵⁶A. M. Ganose, K. T. Butler, A. Walsh and D. O. Scanlon, *J. Mater. Chem. A*, 2016, **4**, 2060–2068.
- ⁵⁷A. Walsh, D. J. Payne, R. G. Egdell and G. W. Watson, *Chem. Soc. Rev.*, 2011, **40**, 4455–4463.
- ⁵⁸A. Walsh and G. W. Watson, *J. Solid State Chem.*, 2005, **178**, 1422–1428.
- ⁵⁹J. P. Allen, J. J. Carey, A. Walsh, D. O. Scanlon and G. W. Watson, *J. Phys. Chem. C*, 2013, **117**, 14759–14769.
- ⁶⁰S. R. Kavanagh, C. N. Savory, D. O. Scanlon and A. Walsh, *Mater. Horiz.*, 2021.
- ⁶¹A. M. Ganose, S. Matsumoto, J. Buckeridge and D. O. Scanlon, *Chem. Mater.*, 2018, **30**, 3827–3835.
- ⁶²T. B. Nasr, H. Maghraoui-Meherzi and N. Kamoun-Turki, *J. Alloys Compd.*, 2016, **663**, 123–127.
- ⁶³W. Qiu, C. Zhang, S. Cheng, Q. Zheng, X. Yu, H. Jia and B. Wu, *J. Solid State Chem.*, 2019, **271**, 339–345.
- ⁶⁴L. D. Whalley, J. M. Frost, B. J. Morgan and A. Walsh, *Phys. Rev. B*, 2019, **99**, 085207.
- ⁶⁵S. G. Albert, *PhD thesis*, Technische Universität München, 2015.
- ⁶⁶K. Zeng, D.-J. Xue and J. Tang, *Semicond. Sci. Technol.*, 2016, **31**, 063001.
- ⁶⁷A. Walsh and A. Zunger, *Nat. Mater.*, 2017, **16**, 964–967.
- ⁶⁸Y. Liu, K. T. E. Chua, T. C. Sum and C. K. Gan, *Phys. Chem. Chem. Phys.*, 2014, **16**, 345–350.
- ⁶⁹Y. Cheng, O. Cojocaru-Mirédin, J. Keutgen, Y. Yu, M. Küpers, M. Schumacher, P. Golub, J.-Y. Raty, R. Dronskowski and M. Wuttig, *Adv. Mater.*, 2019, **31**, 1904316.
- ⁷⁰M. Schubert, T. Hofmann, C. Herzinger and W. Dollase, *Thin Solid Films*, 2004, **455**, 619–623.
- ⁷¹T. B. Nasr, H. Maghraoui-Meherzi, H. B. Abdallah and R. Ben-naceur, *Physica B Condens. Matter.*, 2011, **406**, 287–292.
- ⁷²M. H. Lakhdar, B. Ouni and M. Amlouk, *Mater. Sci. Semicond. Process.*, 2014, **19**, 32–39.
- ⁷³H. Maghraoui-Meherzi, T. B. Nasr and M. Dachraoui, *Mater. Sci. Semicond. Process.*, 2013, **16**, 179–184.
- ⁷⁴A. Lawal, A. Shaari, R. Ahmed and L. Taura, *Curr. Appl. Phys.*, 2018, **18**, 567–575.
- ⁷⁵M. Y. Versavel and J. A. Haber, *Thin Solid Films*, 2007, **515**, 7171–7176.
- ⁷⁶Y. Lai, Z. Chen, C. Han, L. Jiang, F. Liu, J. Li and Y. Liu, *Appl. Surf. Sci.*, 2012, **261**, 510–514.
- ⁷⁷R. Kondrotas, C. Chen, X. Liu, B. Yang and J. Tang, *J. Semicond.*, 2021, **42**, 031701.
- ⁷⁸M. Kumar, N. Umezawa and M. Imai, *Appl. Phys. Express*, 2014, **7**, 071203.